Thermospheric temperatures above Poker Flat, Alaska, during the stratospheric warming event of January and February 2009

M. G. Conde[1] and M. J. Nicolls[2]

Received 29 March 2010; revised 24 August 2010; accepted 26 August 2010; published 24 November 2010.

[1] We report observations of neutral and ion temperatures at approximately 240 km altitude above Poker Flat, Alaska, taken during the stratospheric warming event of January and February 2009. Neutral temperatures were recorded by a single-etalon Fabry-Perot spectrometer observing the nighttime airglow and aurora at 630 nm wavelength, whereas ion temperatures were obtained with the Poker Flat Incoherent Scatter Radar, mostly during daylight. Neutral and ion temperatures generally tracked each other closely; both data sets exhibited a similar overall seasonal trend during January to April 2009 and even showed similar short-term day-to-day fluctuations. Further, the daily fluctuations correlated highly with geomagnetic activity. Both the short-term temperature fluctuations and their overall seasonal trend matched expectations based on the MSIS model evaluated for this period at hourly intervals. A cooling response was seen in neutral temperature over a 2–3 week period during the main phase of the stratospheric warming. The magnitude of this cooling was around 50 K relative to the seasonal trend. A corresponding signature was also discernible in the ion temperatures, although it was less prominent than the neutral response. This was largely because the cooling was masked by ion temperature perturbations driven by magnetic activity. The strength of the response in ion temperature was observed to depend on the local time of the observations, which is consistent with results presented previously.

Citation: Conde, M. G., and M. J. Nicolls (2010), Thermospheric temperatures above Poker Flat, Alaska, during the stratospheric warming event of January and February 2009, *J. Geophys. Res.*, *115*, D00N05, doi:10.1029/2010JD014280.

1. Introduction

[2] Considerable day-to-day variability is observed to occur in Earth's thermosphere and ionosphere above 100 km altitude. This is unsurprising, since the dayside hemisphere at these altitudes is exposed to variable heating by solar ultraviolet radiation, and at high latitudes there is also highly variable deposition of energy and momentum from the solar wind via the magnetosphere. However, there has also been much recent interest in the extent to which thermospheric and ionospheric variability are driven by short-term perturbations (such as waves and tides) that propagate upward from atmospheric layers below [e.g., *Rishbeth and Mendillo*, 2001; *Mendillo et al.*, 2002; *Kazimirovsky*, 2002; *Laštovička*, 2006; *Mukhtarov et al.*, 2010].

[3] One of the most dramatic types of perturbations that occur in the middle atmosphere are sudden stratospheric warmings (SSWs). Upward propagating disturbances associated with these events could presumably be an important driver of variability in the ionosphere and thermosphere during geomagnetically quiet conditions. SSWs are events that occur most strongly in the northern hemisphere's wintertime polar stratosphere, during which the temperature poleward of 60°N suddenly rises by a few tens of Kelvins in less than a week, then recovers over a period of a few weeks. Stratospheric zonal mean winds are also strongly perturbed, reversing to flow easterly during most events. Typical characteristics of SSW events have been reviewed for example by *Andrews et al.* [1987], *Limpasuvan et al.* [2004], and *Krüger et al.* [2005].

[4] Numerous studies have examined how the effects of SSW events propagate upward into the mesosphere and lower thermosphere [e.g., *Nikolashkin et al.*, 2001; *Cho et al.*, 2004; *Dowdy et al.*, 2004; *Azeem et al.*, 2005; *Liu and Roble*, 2005; *Palo et al.*, 2005; *Ignat'ev and Nikolashkin*, 2006; *Sonnemann et al.*, 2006; *Hoffmann et al.*, 2007]. These studies show that the upper mesosphere and lower thermosphere can cool by 20 K to 30 K during and even before an SSW event, that planetary wave activity increases at these heights, and that large westward zonal winds may occur. By contrast, there have been relatively few studies of the effects of SSW events on the middle and upper thermosphere, or on the *F*-region ionosphere. Exceptions include *Bullen* [1964]; *Kazimirovsky* [2002]; *Liu and Roble* [2002]; *Goncharenko and Zhang* [2008].

[1]Geophysical Institute, University of Alaska Fairbanks, Fairbanks, Alaska, USA.
[2]Center for Geospace Studies, SRI International, Menlo Park, California, USA.

0148-0227/10/2010JD014280

[5] Of these, the *Goncharenko and Zhang* [2008] study is most relevant to the present work. They used the Millstone Hill incoherent scatter radar to measure ion temperatures in the height range 100–300 km during local times of daylight and twilight. During the SSW event that occurred in late January 2008 they observed substantial cooling of 20–50 K above 150 km altitude. The cooling was strongest during the local morning and afternoon hours, and peaked at a height of 160–170 km. The *F*-region temperature response was strongly dependent on local time; no significant cooling was seen above 250 km altitude at times around local noon. In contrast to the *F*-region cooling, a substantial 30–50 K warming was seen during local afternoon hours at heights of 120–140 km. The ion temperature at 230 km altitude began decreasing 1–2 days before the onset of rapid warming in the stratosphere. Similar "ionospheric precursor" behaviors have been reported by others, although the *Goncharenko and Zhang* [2008] result was seen in the *F* region.

[6] Here we report on thermospheric neutral temperatures measured at ~240 km altitude above Poker Flat, Alaska using a Fabry-Perot spectrometer, together with ion temperatures measured at the same altitude using the collocated Poker Flat Incoherent Scatter Radar (PFISR). The data shown here cover the period December 2008 through April 2009, which encompasses the strong stratospheric warming that occurred during late January and early February of 2009. The observation period occurred during the deep solar minimum at the end of solar cycle 23, and was characterized by extremely low solar activity and corresponding minimal geomagnetic activity. Although the atmospheric temperature at 240 km altitude still showed clear responses to changing geomagnetic activity, the amplitude of these fluctuations was very low by historical standards. This, coupled with the simultaneous availability of long continuous time series measurements of both neutral and ion temperatures, provided a unique opportunity to look for a possible *F*-region temperature response to the large SSW event that was occurring in the atmosphere below.

2. Instrumentation

2.1. Fabry-Perot Spectrometer

[7] Neutral temperatures were obtained using a single etalon Fabry-Perot spectrometer observing the nighttime airglow and aurora emitted from thermospheric atomic oxygen at a wavelength of 630 nm. This emission originates at night from a layer on the order of 100 km thick peaking typically at around 240 km altitude [e.g., *Rees and Roble*, 1986; *Solomon et al.*, 1988; *Shefov et al.*, 2007]. The Doppler width of the optical emission spectrum at this wavelength has been used since the 1960s [*Wark*, 1960; *Jarrett and Hoey*, 1966; *Roble et al.*, 1968] to infer the temperature of the neutral atmosphere at *F*-region heights. Implicit in this approach is the assumption that the population of atoms radiating at 630 nm is in thermal equilibrium with the ambient neutral atmosphere. While the actual distribution of the radiating population is expected to have a weak enhancement at high temperatures [*Yee*, 1988], its effect is small and is unlikely to significantly bias temperature measurements at auroral latitudes.

[8] The spectrometer used here was an all-sky imaging Fabry-Perot interferometer, first described by *Conde and Smith* [1995, 1997, 1998]. Compared to the instrument described in those papers, the 2009 version featured substantially upgraded optics, imaging detector, and operating software. Nevertheless, its operating principle remains identical. A zenith-centered field of view of the sky extending down to around 75° zenith angle was imaged onto an electron-multiplying CCD detector 8.192 mm square, comprising 512 × 512 pixels. The optical beam was passed at infinite conjugate ratio through a 0.5 nm bandwidth interference filter centered on 630 nm wavelength, and through a Fabry-Perot etalon of 100 mm aperture and 20 mm gap. The resulting image on the detector at any instant of time showed the sky in sharp focus, but angularly modulated in brightness by around 6 orders of the Fabry-Perot interference pattern.

[9] Using the technique described by *Conde and Smith* [1997], the instrument was able to acquire both unmodulated sky images and complete wavelength spectra over its entire field of view, by piezoelectrically "scanning" the etalon gap over time through a range of one whole interference order. Each such scan comprised 128 discrete steps, and took around 24 seconds to complete. Although separate spectra could in principle be obtained for each individual detector pixel, the resulting signal/noise ratio would be unacceptably low. Instead, the field of view was divided into 115 "zones", and spectra were coadded spatially from all pixels within a zone. Each individual observation was obtained by repeating the scan, and coadding the resulting spectra, until the control program determined that the spectra had achieved adequate signal/ratio. The program also enforced requirements for a minimum exposure of 2 scans (0.8 min) and a maximum exposure of 10 min.

[10] Figure 1 illustrates the basic data obtained from one such exposure. It shows the field of view divided into its 115 observing zones, along with individual spectra of the 630 nm emission line for each zone. The spectral interval shown spans just 10 pm in wavelength. The red, green, and blue color channels of the background image are used together to depict how both temperature and emission intensity varied across the sky. Doppler temperatures, derived from the widths of the spectra, are shown using blue through red colors according to the scale bar at the lower left. Green colors depict emission intensity. While the intensity scale is uncalibrated, cross comparison with other instruments indicates that the brightest regions of this image correspond to approximately 2 kilo-Rayleighs of 630 nm emission, which indicates that aurora was present to the north. Whereas only one temperature estimate was obtained per zone, emission intensity estimates were obtained from every detector pixel (although the intensity data shown here have been spatially smoothed slightly to suppress noise.) Yellow arrows depict the horizontal wind field derived from the distribution of Doppler shifts across the sky using the method described by *Conde and Smith* [1998].

[11] Figure 1 shows cooler Doppler temperatures occurring in regions of enhanced auroral brightness. This illustrates one factor complicating the use of 630 nm optical temperatures in the auroral zone. As described by *Sica et al.* [1986], energetic auroral precipitation can enhance 630 nm emission from altitudes below the usual 240 km centroid height of the emission layer. This leads to apparently lower temperatures, due to the thermosphere's positive temperature gradient with height. Thus, although it is tempting to infer from Figure 1

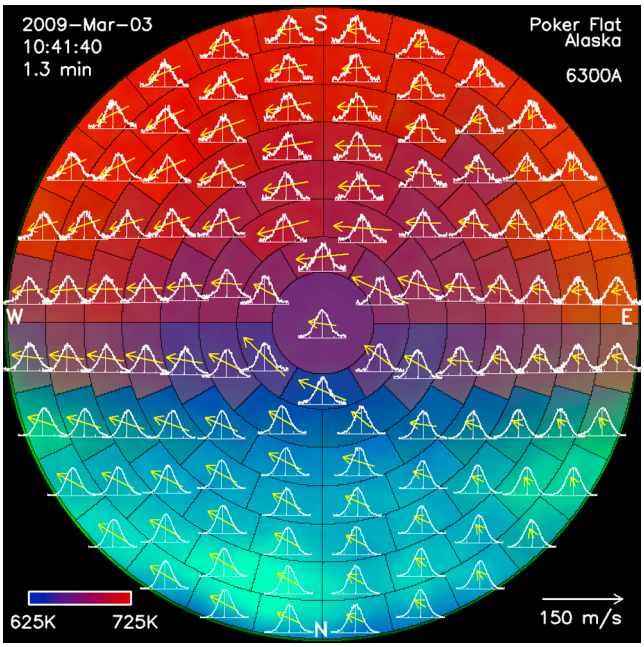

Figure 1. An example of the basic data obtained from one individual Fabry-Perot observation, in this case for a 1.3 min interval centered around 1041:40 UT on 3 March 2009. As described in the text, the background image shows the field of view divided into 115 "zones", with geomagnetic south at the top and east at the right. The spectra acquired from each zone are shown using white curves. Blue through red colors depict the temperatures derived from the spectrum in each zone, according to the color scale bar at the lower left. Green hues depict the 630 nm emission intensity, with the brightest regions corresponding to around 2 kilo-Rayleighs. Yellow arrows depict the fitted horizontal vector wind field.

that there was a southward directed horizontal temperature gradient at 240 km altitude, it is more likely in this case that the data are indicating height variation of the emission layer across the field of view. Such effects are largely suppressed in this study, because our basic conclusions are based on long time series in which each individual data point is a median of all the temperatures from all 115 directions viewed during each exposure.

[12] Temperatures were derived from the observed 630 emission spectra using the method described by *Conde* [2001]. As illustrated in Figure 2, the spectrum observed in each zone was fitted with an emission profile comprising a Gaussian source spectrum convolved with the measured instrument function of the spectrometer in that zone. Four parameters were fitted, corresponding the Gaussian's width, peak wavelength, and total area, along with a DC background term. Temperatures were then derived from the width estimates. Accounting for the effects of instrumental broadening often generates a large fraction of the measurement uncertainty in temperatures derived this way. Here however, the instrument function spectral width's were much narrow (by a factor of ~ 3) than the widths of the observed spectra (see Figure 2). Accounting for instrumental broadening was thus not a major source of uncertainty; the dominant source of uncertainty in an individual measurement was instead merely due to the Poisson noise of the signal counts in each spectral bin.

[13] Absolute calibration of the inferred temperatures depended on absolute knowledge of three quantities: the spectral width of the instrument function, the optical gap between the etalon plates, and the fractional order scanned by the etalon when acquiring spectra. All three of these quantities were known to high relative accuracy. Uncertainty in absolute temperature calibration was therefore small; the approximate absolute temperature uncertainties contributed by these three quantities were just 4, 1, and 1 Kelvins at a nominal temperature of 700 Kelvins.

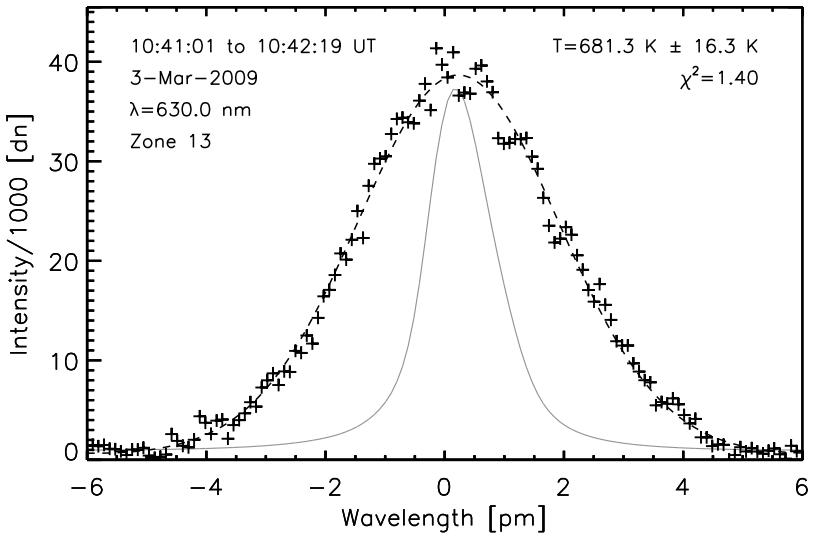

Figure 2. Temperature analysis for one of the spectra shown in Figure 1. In this case the spectrum was accumulated from zone 13, which is located in the "5 o'clock" position on the second ring of zones out from the zenith. Crosses show the observed spectrum, the dashed curve shows the fitted spectrum, and the narrow gray curve shows the instrument function.

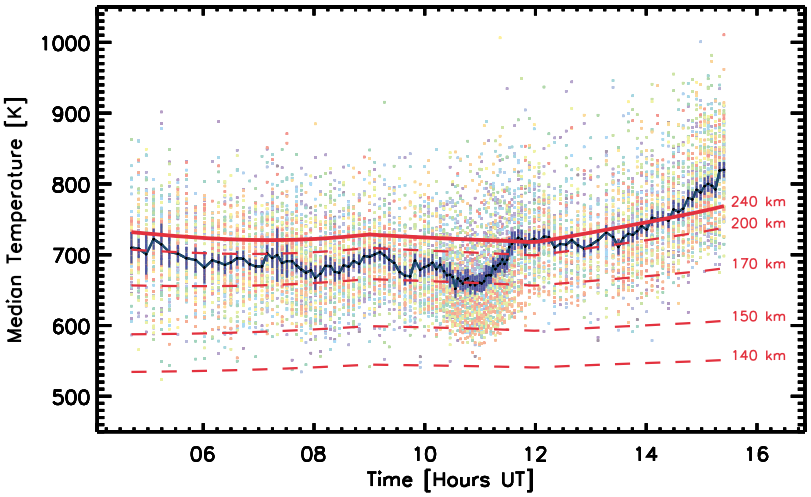

Figure 3. Time series of temperature estimates obtained on the night of 3 March 2009. Vertical columns of colored points depict the sets of 115 temperature measurements obtained from each individual "exposure." The time interval between exposures varied during the night because the instrument adjusts its exposure time according to emission brightness. The heavy black curve depicts the median temperature across all 115 zones. Blue error bars plotted about the black curve show the standard deviation of the median estimates. Red curves depict the MSIS model evaluated at $A_p = 5$ and $F_{10.7} = 70$ for various heights as shown. The heavy red curve shows the MSIS model at the nominal emission height of 240 km.

[14] Figure 3 illustrates how the all-sky data were reduced to a simple time series for use in this study. The individual measurements are shown as pastel colored points, with blue hues denoting observing zones near the zenith, grading to red hues for zones near the edge of the field of view. Data from a single exposure appear as a vertical line of colored points, corresponding to the 115 measurements taken at each time. The points typically scatter over a region spanning roughly ± 100 Kelvins about the nightly temperature trend line, although the density of points is higher near the center. This scatter comprises two contributions; there are genuine geophysical variations across the instrument's field of view, as well as scatter due to the usual measurement uncertainties. The histogram of individual 1σ measurement uncertainties returned by the spectral fitting program peaked on this night at around 30 Kelvins, whereas the 90th percentile occurred at about 50 Kelvins.

[15] The heavy black curve in Figure 3 was obtained by computing the median temperature across all 115 zones during each exposure. Error bars shown about this curve denote the uncertainty in the median temperature at each time, computed from the standard deviation of the 115 measurements divided by $\sqrt{115}$. As well as the basic parameter estimates and their uncertainties, the spectral fitting program returned two parameters related to data quality: the reduced χ^2 of the spectral fit, and an estimate of the signal/noise ratio of the observed spectrum. These parameters were used to reject spectra with weak signal or distorted shapes. (Distorted shapes occur most often as a result of the moon appearing in or near the field of view of an observing zone.) Well over one million individual spectra were acquired during the December 2008 to April 2009 period studied here. Because of the large amount of available data, the thresholds for acceptance were set quite high, so that approximately 10% of all raw observations were rejected. This left 10,424 high-quality median temperature estimates that were concatenated to produce the overall neutral temperature time series used in this study.

2.2. Poker Flat Incoherent Scatter Radar

[16] PFISR is a new UHF (~450 MHz) incoherent scatter radar operating at the Poker Flat Research Range since March of 2007 [*Heinselman and Nicolls*, 2008]. The radar is a phased array capable of beam steering on a pulse-to-pulse basis, and its modern design consisting of 4096 individual antenna element units each with a solid state power amplifier makes remote operations possible. This capability has allowed for unattended, continuous observations of the auroral ionosphere in a low duty cycle (~ 1%), low power consumption mode, capable of producing ionospheric profiles in a reduced set of look directions at roughly 15 min cadence. This mode was originally instigated as part of the International Polar Year (March 2007 through March 2008) [*Sojka et al.*, 2007, 2009a] but has continued as a basic background diagnostic tool since that time. The original operations through September of 2007 consisted of a single look direction up the local magnetic field line (elevation of ~ 77.5°, azimuth of ~ −154.3°), after which additional look directions were added to allow for local electric field estimates as well. In addition to these low duty cycle measurements, typical PFISR full duty cycle operations include a beam pointed in the direction of the local magnetic line; these have been included in the data set presented in this paper to allow for a nearly continuous set of ionospheric measurements, except for a period from 12 December 2008 through 8 January 2009 when a system failure precluded measurements. The pulse scheme for this "IPY" mode consists of interleaved 480 μs long pulses and 16-baud, 30 μs baud alternating code pulses (see *Sojka et al.* [2009a] for more details).

[17] For the data presented in this paper, both the long pulse and alternating code were sampled at 30 μs and lag profiles

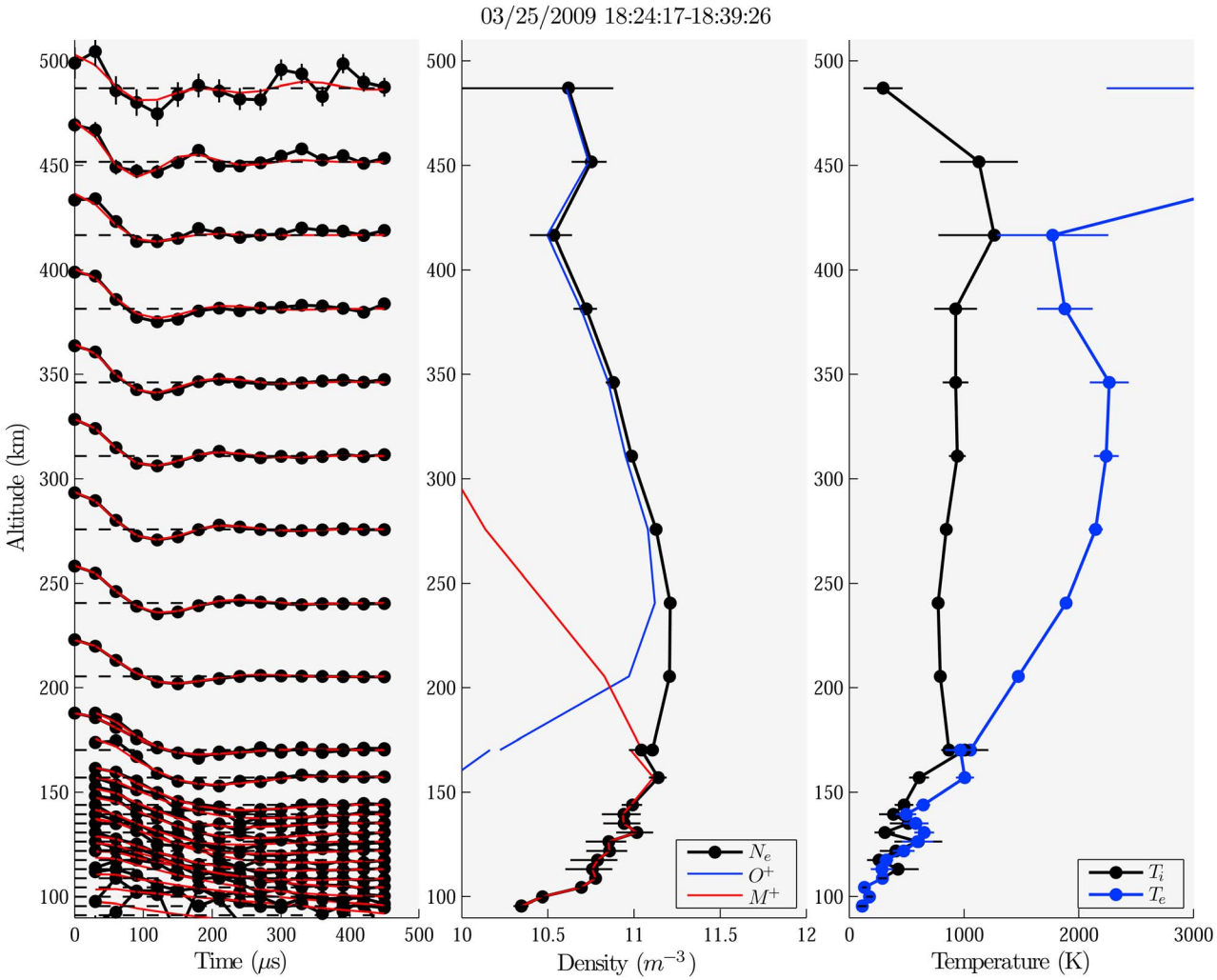

Figure 4. For a 15 min period near 1830 UT on 25 March 2009. (left) Real part of autocorrelation function (black points with error bars) and fitted curves (red) from 80 to 500 km, using the alternating code up to 175 km and the long pulse above that point. (middle) Fitted electron density (black points), derived molecular ion density (red), and derived O+ density (blue). (right) Fitted ion (black) and electron (blue) temperature.

in range are computed. Summation rules were applied to the long-pulse profiles to produce autocorrelation function (ACF) estimates every ~half pulse width with roughly equivalent range smearing for all lags. For the alternating code, this is not necessary, and data were only integrated in range to improve the statistics of the measurements. The complex ACFs were then fit for ionospheric parameters including electron and ion temperatures (T_e and T_i), electron density (N_e), and line-of-sight drift speeds (V_{los}) using a standard incoherent scatter formulation [e.g., *Evans*, 1969] taking into account the lag ambiguity function of the pulse sequence, which was calculated using the true digital filter specification. The fits are sensitive to an absolute system calibration, which was obtained using injected calibration pulses of known temperature in addition to simultaneous plasma line measurements during the daytime (often, but not always, available). The fits can also be sensitive to some parameters not directly measured, such as ion-neutral collision frequency at *E*-region altitudes and ion composition in the lower *F* region. Collision frequencies were calculated using empirical formulas and MSIS neutral densities, and the molecular ion composition was obtained using an iterative approach based on a chemical model formulated in terms of N_e, T_i, T_e, and T_n, as described by *Richards et al.* [2009]. One example of a derived profile is shown in Figure 4. Figure 4 (left) shows an altitude profile of a measured ACF (black points, real part only) along with the model fits (red curve). Here we used the alternating code ACFs up to about 175 km and the long-pulse ACFs above that point. Figure 4 (middle) shows the derived N_e (black points) along with the calculated O^+ (blue) and molecular ion (M^+) fraction (red). Figure 4 (right) shows the derived electron and ion temperatures. For this study, we were mainly interested in thermospheric ion temperatures and only utilized measurements from the long pulse centered at ~240 km.

[18] Two sets of 24 h observations separated by one day are shown in Figure 5 to illustrate how data were combined, as well as the differences between quiet and (locally) active time periods. These days correspond to 25 March 2009 (daily average K_p index of ~2) and 27 March 2009 (daily average K_p

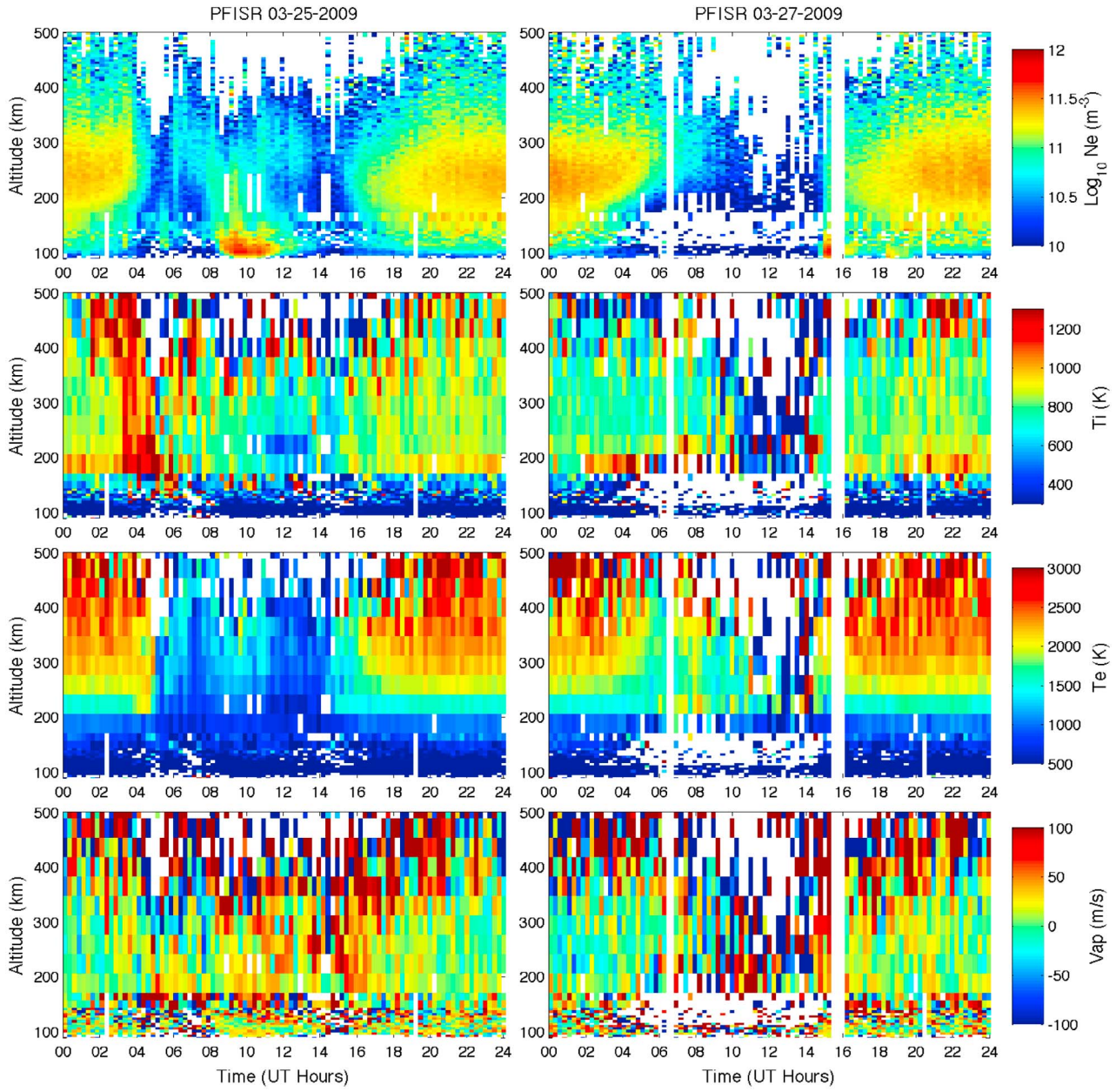

Figure 5. Ionospheric parameters for two 24 h periods on (left) 25 March and (right) 27 March. From top to bottom: electron density, ion temperature, electron temperature, and line of sight drift speed.

index of ~1). Figure 5 top to bottom plots correspond to electron density, ion temperature, electron temperature, and line-of-sight ion speed. The day 25 March consisted of a continuous time series from a single experiment, whereas 27 March included daytime observations in one operating mode and nighttime operations in another (delineated by the white data gaps where the experiment transitioned). Electron densities showed a clear precipitation signature on 25 March and no such signature on 27 March. The ion temperatures on 25 March were enhanced due to the start of the geomagnetic activity, which coincided with a period of enhanced westward convection (not shown) that contributed to ion heating. Nighttime temperatures could be deduced on this day as a result of the nighttime *F*-region ionization caused by soft precipitation. On 27 March, on the other hand, the nighttime temperatures were not reliable because of the extremely low electron densities (and resulting low signal to noise ratios). Because the period under investigation in this study fell during a time of exceptionally low solar flux and geomagnetic activity, reliable nighttime temperatures were not common. Further, when they were available, they may not have been representative of the background state of the thermosphere because of enhanced ion heating from electric fields.

[19] For this study, data were available at intervals of roughly 15 min during periods when operations were compatible with ion temperature measurements up the local magnetic field line. Temperatures were eliminated when errors (returned by the nonlinear least squares fitter) were

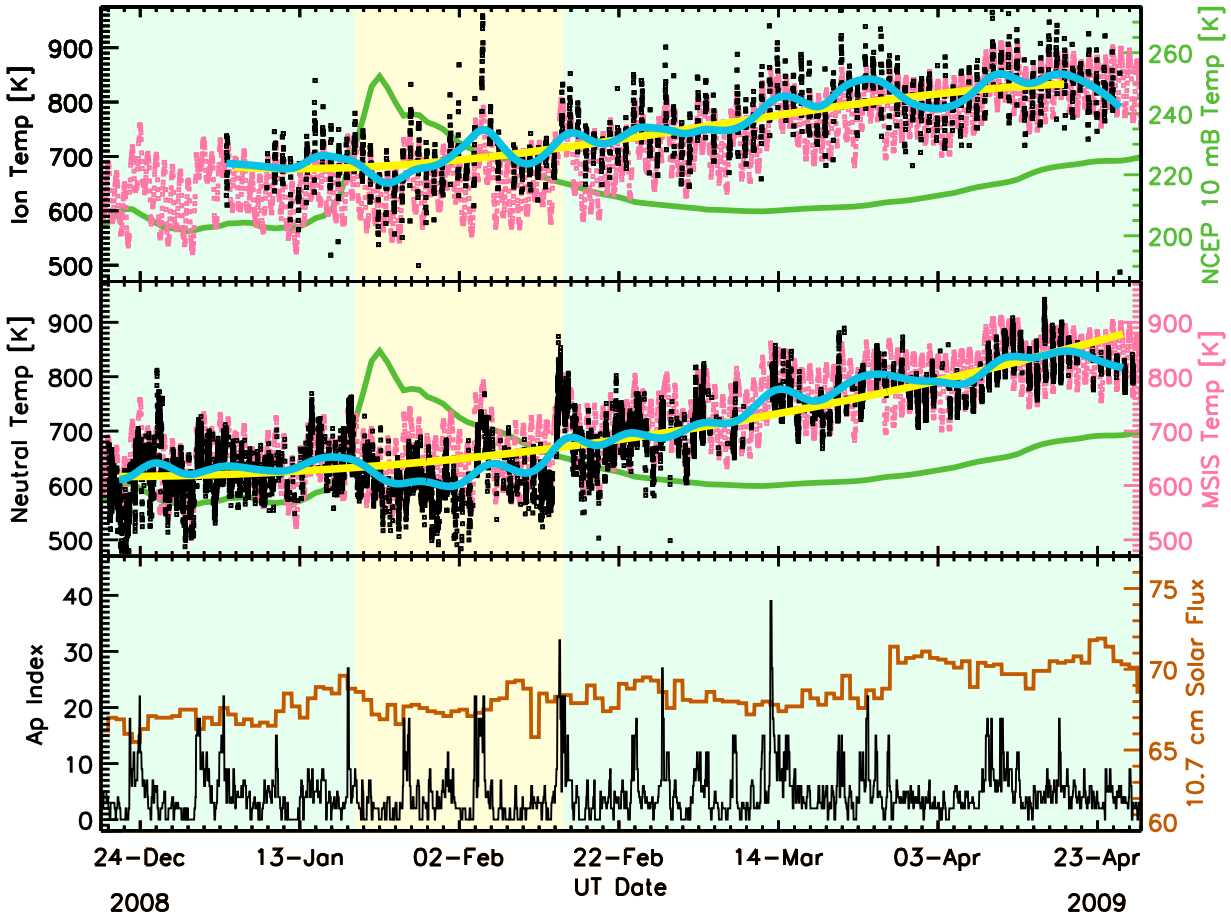

Figure 6. (top) Ion and (middle) neutral temperature observations for the whole study period, overlaid onto temperature estimates from the MSIS model evaluated hourly using (bottom) the appropriate A_p and $F_{10.7}$ values at each time. Green curves depict NCEP temperatures on the 10 hPa isobaric surface above Poker Flat. Blue curves in Figure 6 (top and middle) depict smoothed trends through the ion and neutral data, whereas yellow curves depict cubic polynomial fits to these data. A change in background shading (from blue to yellow) is used to highlight the period of stratospheric warming.

large (greater than 30% or 100 K) or when number densities were low (less than 3×10^{10} m^{-3}).

3. Observations

[20] Figure 6 shows a compilation of the data acquired for this study. Black points in Figure 6 (top) show PFISR ion temperatures from 240 km altitude, superimposed on pink points that depict MSIS-90 model [*Hedin*, 1991] temperatures calculated hourly using the observed 10.7 cm solar flux and A_p geomagnetic index data. The blue curve is an interpolated and heavily smoothed "fit" through the individual ion temperature points. The yellow curve is a third-order polynomial fit to the ion temperature data; it indicates the overall temperature trend on even longer time scales. The green curve depicts NCEP temperature data for this period on the 10 hPa isobaric surface above Poker Flat. The prominent peak in this curve indicates the period when the stratospheric warming was in progress.

[21] Figure 6 (middle) uses a similar format to Figure 6 (top), but in this case it shows the Fabry-Perot neutral temperatures, together with the trend lines due to smoothing and polynomial fitting. The NCEP 10 hPa temperatures are once again plotted in green behind the thermospheric temperature data, as are the hourly MSIS-90 neutral temperatures (pink). Figure 6 (bottom) shows time series plots of the daily 10.7 cm solar flux and of the 3-hourly magnetic A_p index. Figure 6 allows individual neutral and ion temperatures to be compared with MSIS temperatures evaluated at 240 km altitude at hourly intervals, using the actual time history of solar flux and magnetic A_p index that prevailed during the observations.

[22] Figure 7 essentially replots the data from Figure 6, but now with the neutral (red) and ion (blue) temperatures and their respective trends all in the same panel. While the individual MSIS points have been omitted from this plot for clarity, the green curve instead shows the smoothed trend that was fitted through the MSIS model data. The black curve here shows the NCEP temperature data at 10 hPa, whereas the gray bar graph plot at the bottom depicts magnetic activity using the K_p index (rather than A_p, which was used in Figure 6). Slightly less aggressive smoothing was applied to the Fabry-Perot data shown in Figure 7, relative to that used to generate Figure 6. As a result, the smoothed Fabry-Perot curve in

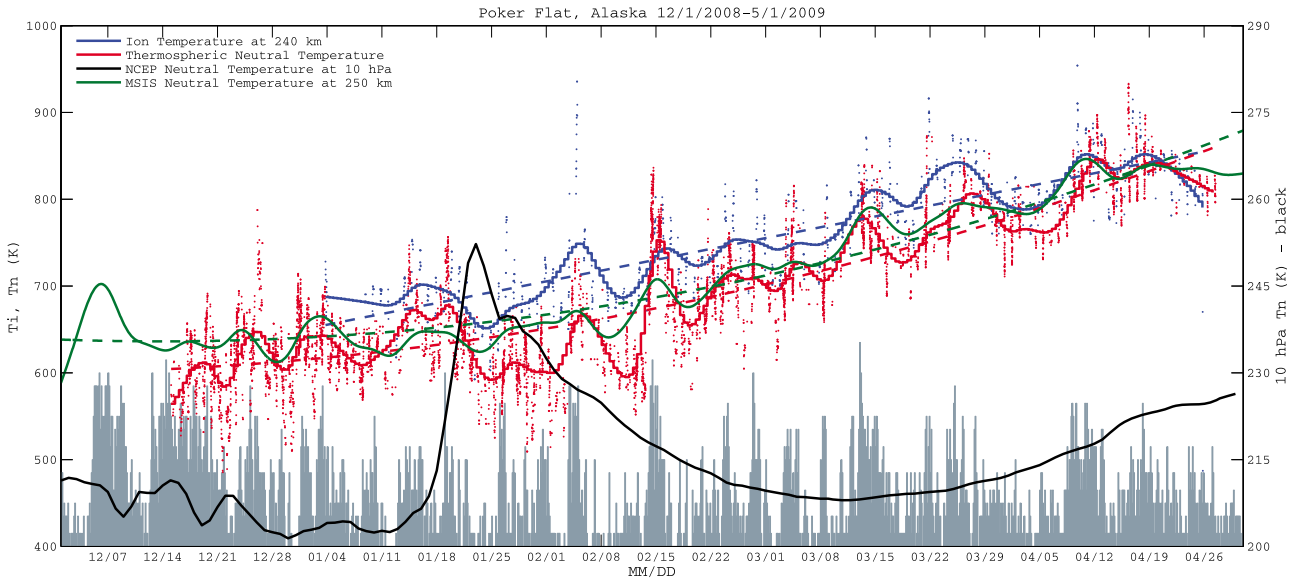

Figure 7. Comparison of PFISR 240 km T_i (blue), FPS T_n (red), and MSIS 250 km T_n (green) from 1 December 2008 to 1 May 2009. Individual data points and smoothed trends are shown. The 3 h K_p index is shown as bars (scaling of $50 \times K_p + 400$ K has been applied) and the NCEP 10 hPa is shown in black (axis on right).

Figure 7 follows the short-term temperature fluctuations rather more closely.

[23] The salient features of Figures 6 and 7 are as follows.

[24] 1. The two observational data sets (neutral and ion temperature) and the MSIS model all show quite similar mean values over the interval studied. Even so, a persistent small difference was observed between the ion and neutral temperatures, with the ions being slightly hotter than the neutrals. This is consistent with the expected sign of the ion-neutral temperature difference, especially given that most of the ion temperature measurements were made during the daytime, whereas most of the neutral temperature measurements were made at night. These results suggest that the absolute calibrations of both the ion and neutral temperature measurements were reasonable.

[25] 2. All three time series exhibited a similar trend of rising temperature as the season advanced from midwinter into the northern spring. It is noted, however, that the seasonal slope of the ion temperatures was slightly less than those of either the MSIS model or the Fabry-Perot data. The shallower slope in the ion temperatures arose because at the start of our data period the ions were slightly hotter relative to the neutrals than they were at the end of the period.

[26] 3. While individual measurements of ion or neutral temperature do not exactly match the hourly MSIS data points, the general locations of the points in all three data sets track each other remarkably well. This is even more apparent when comparing the red, green, and blue curves of smoothed data that are shown in Figure 7. It is obvious even from a qualitative assessment by eye that the various oscillations are not only well correlated between these (experimentally independent) curves, they are also well correlated with the A_p and K_p indices.

[27] 4. During the SSW period, it appears that at least the neutral temperatures at 240 km altitude did show a significant negative offset, which was around −50 K relative to the overall seasonal trend. Short-term perturbations in ion temperature during the SSW period were consistent with those of the neutral temperature, although in this case the data do not appear to show an overall net cooling.

4. Discussion

[28] The historical record of 10.7 cm solar radio flux and magnetic A_p index shows that our observations were taken during a period when solar and geomagnetic activity levels were at or below those of the deepest minima that have occurred any time during the preceding 5 to 6 solar cycles. While the 10.7 cm radio flux during the 2009 northern spring was comparable to that observed at the bottoms of each of the preceding few solar cycles,the A_p index shows that magnetic activity was actually lower than at virtually any time since 1940. The length and depth of this current solar minimum were unexpected, and they have become the subject of many current investigations.

[29] Nevertheless, apart from the obvious seasonal trend, the most prominent geophysical feature in our observational data is the highly correlated response of both neutral and ion temperature to short-term fluctuations in geomagnetic activity. This response was the dominant source of day-to-day variability, despite the quiet conditions. We presume that similar observations taken during periods of moderate or high solar and magnetic activity would typically contain similar fluctuations, but with substantially increased amplitude. It therefore seems unlikely that thermospheric responses to SSW events would be discernible during other (more active) phases of the solar cycle.

[30] The temperature oscillations seen here are reminiscent of the quasi-periodic density fluctuations at 400 km altitude reported by *Lei et al.* [2008] and *Thayer et al.* [2008]. Those density oscillations were identified as a thermospheric response to Earth's repetitive encounters with long-lived

corotating interaction regions (CIRs) in the solar wind, and we are currently undertaking a study to establish whether the same is true for the ion and neutral temperature oscillations seen during the present study. Signatures of CIR activity have indeed been observed previously in PFISR ion temperature measurements, based on data from the IPY period of March 2007–2008; a one-to-one relation was found between CIR activity and T_i response [*Sojka et al.*, 2009b].

[31] While oscillations driven by time-varying magnetic activity might partially obscure any temperature response to the SSW event, they nevertheless did offer one useful side effect. That is, they gave a naturally provided "test signal" that we could use to verify our two instruments' ability to resolve small temperature perturbations. As seen in Figure 7, the neutral and ion temperature fluctuations not only correlated highly with each other over many oscillation cycles, they also correlated equally well with the oscillation we would expect to see, based on MSIS. Such a three-way correlation over this many cycles would be extraordinarily unlikely if the small perturbations seen by our instruments were solely due to random noise. We are therefore very confident of both instruments' ability to resolve actual variations in temperature at a level of 50 Kelvins or so.

[32] This then brings us to the stratospheric warming event. Figures 6 and 7 show that neutral temperatures during the period from late January to mid February were depressed by something like 50 Kelvins relative to their long-term trend. This can be seen easily in either Figure 6 or Figure 7 by comparing the smoothed neutral temperature data with the corresponding polynomial fit to it. Even without the fits, it is also apparent from Figure 6 (middle) that during this period more of the individual neutral temperature observations (black) fell below the MSIS model temperatures (pink) than was typical at other times.

[33] The NCEP temperatures at 10 hPa shown in Figures 6 and 7 also indicate that the period of depressed neutral temperature at 240 km altitude corresponded very closely to the main phase of the stratospheric warming event. There were three periods of weakly elevated magnetic activity during the SSW event; they occurred around 26 January, 5 February, and 14 February. Enhancements of neutral and ion temperatures were observed in response to all three of these events, and they do act to some extent to obscure the neutral temperature response to the SSW. For example, it is not clear when the cooling signature of SSW actually ended in the neutral temperature data, because the end of the SSW event coincided with a period of enhanced geomagnetic activity.

[34] Despite these complications, it does seem likely that effects of this stratospheric warming event did indeed extend into the middle thermosphere, where they manifested as a three week cooling by approximately 50 Kelvins. This conclusion is supported first by the temporal coincidence between events seen in the NCEP and Fabry-Perot data, and secondly by the evidence that the Fabry-Perot can indeed resolve real geophysical temperature fluctuations at the 50 Kelvin level. Unlike previous studies of cooling at mesospheric and lower thermospheric heights, we saw no indication that the cooling at 240 km altitude was a precursor to warming in the stratosphere below. There are of course several other brief periods when observed temperatures dipped below those predicted by the MSIS model. The most notable of these occurred during the last week or so of observations, when both neutral and ion temperatures dipped sharply downward. Such periods are fully expected when fitting an empirical model like MSIS to a naturally variable system like the thermosphere. They do however raise the question of whether the cooler thermospheric temperatures seen during January and February were just another stochastic oscillation, coincident in time with the SSW event, but not causally related to it. While there is no definitive way to dismiss this possibility, we note that the cooling during the SSW lasted conspicuously longer (by at least a factor of 2) than any other temperature perturbation seen during the observation period, which suggests to us that this event was more than just another random fluctuation.

[35] The remaining question is whether the SSW event drove a corresponding (cooling) response in the ion temperatures. Figure 6 (top) does not appear to show any identifiable cooling response during the SSW. By contrast, the smoothed ion temperature curve shown in Figure 7 does suggest that some cooling actually did occur during the SSW period, and that it correlated quite well with the neutral cooling. The reason why Figures 6 and 7 appear to tell slightly different stories is because they use slightly different polynomial fits to draw the trend lines, which make the negative perturbation appear more obvious in Figure 7.

[36] Even so, it is clear that the cooling is less prominent in the ion temperatures than it is in the neutrals. This is likely because of the coincident CIR activity, to which the ions responded strongly. It is notable that the start of the SSW coincided with a period of low geomagnetic activity and, indeed, during this time cooling was observed in both the ions and neutrals of roughly the same magnitude from the trend line (~50 K).

[37] The radar data shown so far were compiled from observations taken at all local times, but with a strong bias toward daytime periods. (This daytime bias arises due to the stronger back-scattered radar power that is typically received from the sunlit ionosphere; nighttime electron densities in the quiescent polar ionosphere are extremely low.) Recall that the *Goncharenko and Zhang* [2008] study showed that cooling at 240 km altitude above their site depended strongly on local time. They clearly saw cooling during the morning and evening hours, but not during times around local noon. To test whether local time was a factor in the Poker Flat ion temperatures, we divided our radar data into three local-time-based subsets, corresponding to night time (1900–0800 LST), ~ local noon (1000–1400 LST) time, and all data. Figure 8 shows (smoothed) ion temperatures from each subset (brown, green, and blue), along with Fabry-Perot neutral temperatures overlaid for visual reference (red). Note that the ion temperatures have been less aggressively smoothed here than they were in Figures 6 and 7. In addition, a local time histogram of the data points is shown (right) as well as a time series showing the number of data points in each 24 h period. Figure 8 (bottom left) clearly shows the issues at play; while the number of useful data points around local noon is relatively constant over the whole period, the numbers of points at night is strongly tied to K_p: during times of elevated K_p there was higher likelihood of precipitation-enhanced electron densities occurring within the PFISR field of view. Nevertheless, some inferences can be drawn. As expected, the mean daytime temperatures (green) are higher than the overall mean (blue) but still show a strong response to

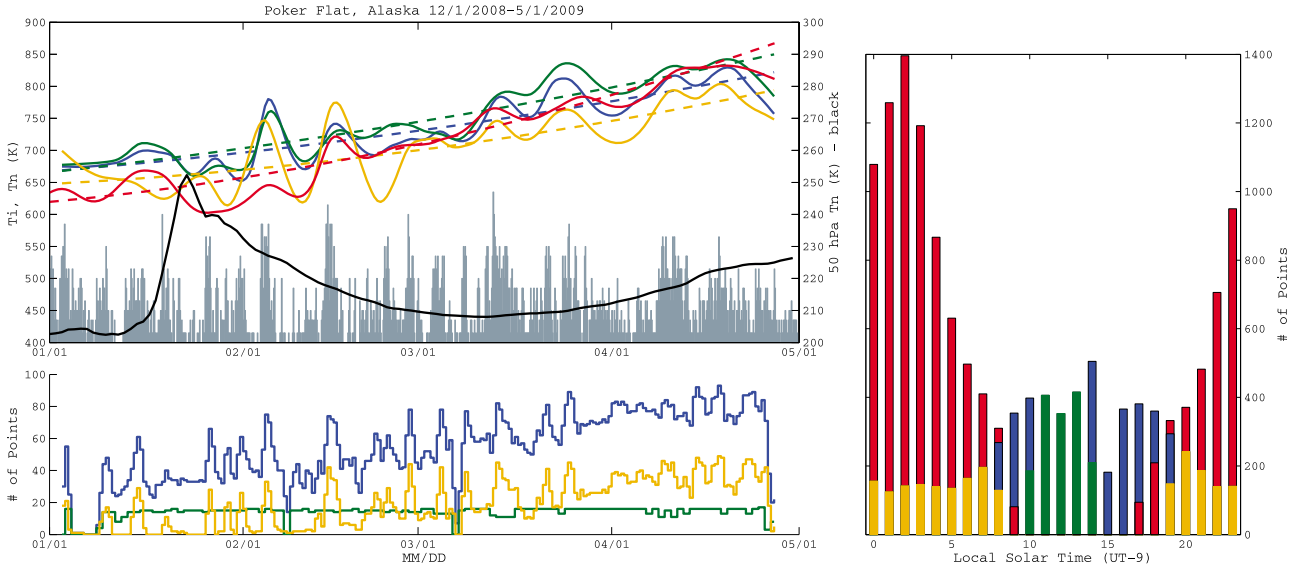

Figure 8. (top left) Smoothed versions of PFISR T_i binned in three time periods: all data (blue), 1000–1400 LST (green), 1900–0800 LST (brown). The red curve is a smoothed version of the FPS T_n. (bottom Left) Number of points for each curve in a given 24 h period for the time series. (right) Histogram of data points in local time.

geomagnetic activity, indicating that the temperatures remain elevated even during the daytime. The nighttime temperatures are overall much cooler than the daytime temperatures, but show a strong response to geomagnetic activity for the reasons given above (both geophysics and sampling issues). While none of the subsets displayed a cooling during the SSW event that was as obvious as that seen in the neutrals, the daytime-only ion temperatures do follow the night time neutral temperatures more closely during the SSW event than do the unsorted ion temperatures in Figure 7. This is especially true during the first week or so of the SSW event. The major difference between the daytime ion temperature and the nighttime neutral temperature in Figure 8 is that the ion temperatures responded much more strongly to the magnetic activity that occurred around 5 and 14 February than the neutrals did, which is hardly surprising. Thus our current study suggests that the ionospheric temperature signature of an SSW event can be obscured even more easily by geomagnetic forcing than is the case for the neutrals.

5. Conclusions

[38] Measurements of neutral temperature at 240 km altitude above Poker Flat clearly show that the thermosphere cooled at this location by around 50 K during the stratospheric warming event of late January and early February 2009. A corresponding perturbation was also discernible in simultaneous measurements of ion temperature, especially for the early part of the SSW period. However the cooling signature was less apparent in the ion data than in the neutrals, most likely because the ion cooling was partially obscured by heating in response to geomagnetic activity. The ion temperature response was observed to depend on local time, consistent with results obtained by previous workers. Well-correlated quasi-periodic neutral and ion temperature perturbations were seen throughout the observing period. These perturbations also correlated closely with periods of magnetic disturbance. Based on our instruments' demonstrated ability to resolve the fluctuations driven by geomagnetic activity, we are confident that the cooling event that appears in our data reflects a real perturbation of thermospheric temperature, and is not the result of measurement noise.

[39] **Acknowledgments.** Data collection and analysis for the PFISR radar were supported under NSF cooperative agreement ATM-0608577 to SRI International. Data collection and analysis for the Poker Flat Fabry-Perot spectrometer were supported under NSF grant ATM-0737618 to the Geophysical Institute of the University of Alaska Fairbanks. We thank the staff of Poker Flat Research Range for supporting observations with these two instruments.

References

Andrews, D. G., J. R. Holton, and C. B. Leovy (1987), *Middle Atmosphere Dynamics*, *Int. Geophys. Ser.*, vol. 40, Academic, San Diego, Calif.

Azeem, S. M. I., E. R. Talaat, G. G. Sivjee, H. Liu, and R. G. Roble (2005), Observational study of the 4-day wave in the mesosphere preceding the sudden stratospheric warming events during 1995 and 2002, *Geophys. Res. Lett.*, *32*, L15804, doi:10.1029/2005GL023393.

Bullen, J. M. (1964), Ionospheric recombination and the polar stratospheric warming, *J. Atmos. Terr. Phys.*, *26*, 559–562, doi:10.1016/0021-9169(64)90187-4.

Cho, Y., G. G. Shepherd, Y. Won, S. Sargoytchev, S. Brown, and B. Solheim (2004), MLT cooling during stratospheric warming events, *Geophys. Res. Lett.*, *31*, L10104, doi:10.1029/2004GL019552.

Conde, M. (2001), Analysis of Fabry-Perot spectra of lidar backscatter echoes, *Anare Rep.*, *146*, 91–114.

Conde, M., and R. W. Smith (1995), Mapping thermospheric winds in the auroral zone, *Geophys. Res. Lett.*, *22*, 3019–3022, doi:10.1029/95GL02437.

Conde, M., and R. W. Smith (1997), Phase compensation of a separation scanned, all-sky imaging Fabry Perot spectrometer for auroral studies, *Appl. Opt.*, *36*, 5441–5450, doi:10.1364/AO.36.005441.

Conde, M., and R. W. Smith (1998), Spatial structure in the thermospheric horizontal wind above Poker Flat, Alaska, during solar minimum, *J. Geophys. Res.*, *103*, 9449–9472, doi:10.1029/97JA03331.

Dowdy, A. J., R. A. Vincent, D. J. Murphy, M. Tsutsumi, D. M. Riggin, and M. J. Jarvis (2004), The large-scale dynamics of the mesosphere-

lower thermosphere during the Southern Hemisphere stratospheric warming of 2002, *Geophys. Res. Lett.*, *31*, L14102, doi:10.1029/2004GL020282.
Evans, J. V. (1969), Theory and practice of ionosphere study by Thomson scatter radar, *Proc. IEEE*, *57*, 498–530.
Goncharenko, L., and S. Zhang (2008), Ionospheric signatures of sudden stratospheric warming: Ion temperature at middle latitude, *Geophys. Res. Lett.*, *35*, L21103, doi:10.1029/2008GL035684.
Hedin, A. E. (1991), Extension of the MSIS thermosphere model into the middle and lower atmosphere, *J. Geophys. Res.*, *96*, 1159–1172, doi:10.1029/90JA02125.
Heinselman, C. J., and M. J. Nicolls (2008), A Bayesian approach to electric field and E-region neutral wind estimation with the Poker Flat Advanced Modular Incoherent Scatter Radar, *Radio Sci.*, *43*, RS5013, doi:10.1029/2007RS003805.
Hoffmann, P., W. Singer, D. Keuer, W. K. Hocking, M. Kunze, and Y. Murayama (2007), Latitudinal and longitudinal variability of mesospheric winds and temperatures during stratospheric warming events, *J. Atmos. Sol. Terr. Phys.*, *69*, 2355–2366, doi:10.1016/j.jastp.2007.06.010.
Ignat'ev, V. M., and S. V. Nikolashkin (2006), Temperature disturbances in the subauroral lower thermosphere during winter stratospheric warming, *Geomagn. Aeron.*, *46*, 214–217, doi:10.1134/S0016793206020101.
Jarrett, A. H., and M. J. Hoey (1966), Observations of the 6300 Å OI nightglow emission, *J. Atmos. Terr. Phys.*, *28*, 175–183, doi:10.1016/0021-9169(66)90115-2.
Kazimirovsky, E. S. (2002), Coupling from below as a source of ionospheric variability: A review, *Ann. Geophys.*, *45*, 1–29.
Krüger, K., B. Naujokat, and K. Labitzke (2005), The unusual midwinter warming in the Southern Hemisphere stratosphere 2002: A comparison to Northern Hemisphere phenomena, *J. Atmos. Sci.*, *62*, 603–613, doi:10.1175/JAS-3316.1.
Laštovička, J. (2006), Forcing of the ionosphere by waves from below, *J. Atmos. Sol. Terr. Phys.*, *68*, 479–497, doi:10.1016/j.jastp.2005.01.018.
Lei, J., J. P. Thayer, J. M. Forbes, E. K. Sutton, and R. S. Nerem (2008), Rotating solar coronal holes and periodic modulation of the upper atmosphere, *Geophys. Res. Lett.*, *35*, L10109, doi:10.1029/2008GL033875.
Limpasuvan, V., D. W. J. Thompson, and D. L. Hartmann (2004), The life cycle of the Northern Hemisphere sudden stratospheric warmings, *J. Clim.*, *17*, 2584–2597, doi:10.1175/1520-0442(2004)017.
Liu, H., and R. G. Roble (2002), A study of a self-generated stratospheric sudden warming and its mesospheric-lower thermospheric impacts using the coupled TIME-GCM/CCM3, *J. Geophys. Res.*, *107*(D23), 4695, doi:10.1029/2001JD001533.
Liu, H., and R. G. Roble (2005), Dynamical coupling of the stratosphere and mesosphere in the 2002 Southern Hemisphere major stratospheric sudden warming, *Geophys. Res. Lett.*, *32*, L13804, doi:10.1029/2005GL022939.
Mendillo, M., H. Rishbeth, R. G. Roble, and J. Wroten (2002), Modelling F2-layer seasonal trends and day-to-day variability driven by coupling with the lower atmosphere, *J. Atmos. Sol. Terr. Phys.*, *64*, 1911–1931, doi:10.1016/S1364-6826(02)00193-1.
Mukhtarov, P., B. Andonov, C. Borries, D. Pancheva, and N. Jakowski (2010), Forcing of the ionosphere from above and below during the Arctic winter of 2005/2006, *J. Atmos. Sol. Terr. Phys.*, *72*, 193–205, doi:10.1016/j.jastp.2009.11.008.
Nikolashkin, S. V., V. M. Ignatyev, and V. A. Yugov (2001), Response of the subauroral lower thermospheric and mesopause temperatures on strong polar stratosphere winter warming, *J. Atmos. Sol. Terr. Phys.*, *63*, 859–863, doi:10.1016/S1364-6826(00)00208-X.
Palo, S. E., J. M. Forbes, X. Zhang, J. M. Russell, C. J. Mertens, M. G. Mlynczak, G. B. Burns, P. J. Espy, and T. D. Kawahara (2005), Planetary wave coupling from the stratosphere to the thermosphere during the 2002 Southern Hemisphere pre-stratwarm period, *Geophys. Res. Lett.*, *32*, L23809, doi:10.1029/2005GL024298.
Rees, M. H., and R. G. Roble (1986), Excitation of O(1D) atoms in aurorae and emission of the forbidden OI 6300-A line, *Can. J. Phys.*, *64*, 1608–1613.
Richards, P. G., M. J. Nicolls, C. J. Heinselman, J. J. Sojka, J. M. Holt, and R. R. Meier (2009), Measured and modeled ionospheric densities, temperatures, and winds during the International Polar Year, *J. Geophys. Res.*, *114*, A12317, doi:10.1029/2009JA014625.
Rishbeth, H., and M. Mendillo (2001), Patterns of F2-layer variability, *J. Atmos. Sol. Terr. Phys.*, *63*, 1661–1680, doi:10.1016/S1364-6826(01)00036-0.
Roble, R. G., P. B. Hays, and A. F. Nagy (1968), Calculated [OI] 6300 Å nightglow doppler temperatures for solar cycle minimum, *Planet. Space Sci.*, *16*, 1109–1113, doi:10.1016/0032-0633(68)90123-2.
Shefov, N. N., A. I. Semenov, and O. T. Yurchenko (2007), Empirical model of the OI 630 nm emission variations. 3. Emitting layer height, *Geomagn. Aeron.*, *47*, 750–755, doi:10.1134/S0016793207060072.
Sica, R. J., M. H. Rees, G. J. Romick, R. G. Roble, and G. Hernandez (1986), The altitude region sampled by ground-based Doppler temperature measurements of the OI 15867 K emission line in aurorae, *Planet. Space Sci.*, *34*, 483–488, doi:10.1016/0032-0633(86)90035-8.
Sojka, J., R. Schunk, T. van Eyken, J. Kelly, C. Heinselman, and M. McCready (2007), Ionospheric Challenges of the International Polar Year, *Eos Trans. AGU*, *88*, 171–171, doi:10.1029/2007EO150003.
Sojka, J. J., M. J. Nicolls, C. J. Heinselman, and J. D. Kelly (2009a), The PFISR IPY observations of ionospheric climate and weather, *J. Atmos. Sol. Terr. Phys.*, *71*, 771–785, doi:10.1016/j.jastp.2009.01.001.
Sojka, J. J., R. L. McPherron, A. P. van Eyken, M. J. Nicolls, C. J. Heinselman, and J. D. Kelly (2009b), Observations of ionospheric heating during the passage of solar coronal hole fast streams, *Geophys. Res. Lett.*, *36*, L19105, doi:10.1029/2009GL039064.
Solomon, S. C., P. B. Hays, and V. J. Abreu (1988), The auroral 6300 Å emission: Observations and modeling, *J. Geophys. Res.*, *93*, 9867–9882, doi:10.1029/JA093iA09p09867.
Sonnemann, G. R., M. Grygalashvyly, and U. Berger (2006), Impact of a stratospheric warming event in January 2001 on the minor constituents in the MLT region calculated on the basis of a new 3D-model LIMA of the dynamics and chemistry of the middle atmosphere, *J. Atmos. Sol. Terr. Phys.*, *68*, 2012–2025, doi:10.1016/j.jastp.2006.04.005.
Thayer, J. P., J. Lei, J. M. Forbes, E. K. Sutton, and R. S. Nerem (2008), Thermospheric density oscillations due to periodic solar wind high-speed streams, *J. Geophys. Res.*, *113*, A06307, doi:10.1029/2008JA013190.
Wark, D. Q. (1960), Doppler widths of the atomic oxygen lines in the airglow, *Astrophys. J.*, *131*, 491–501, doi:10.1086/146854.
Yee, J. (1988), Non-thermal distribution of O(1D) atoms in the night-time thermosphere, *Planet. Space Sci.*, *36*, 89–97, doi:10.1016/0032-0633(88)90149-3.

M. G. Conde, Geophysical Institute, University of Alaska Fairbanks, 903 Koyukuk Dr., Fairbanks, AL 99775, USA. (mark.conde@gi.alaska.edu)
M. J. Nicolls, Center for Geospace Studies, SRI International, 333 Ravenswood Ave., Menlo Park, CA 94025, USA. (michael.nicolls@sri.com)